

# Automated Extrinsic Calibration for 3D LiDARs with Range Offset Correction using an Arbitrary Planar Board

Junha Kim, Changhyeon Kim, Youngsoo Han and H. Jin Kim

**Abstract**—This paper proposes an automatic and accuracy-enhanced extrinsic calibration method for 3D LiDARs with a range offset correction, which needs only an arbitrarily-shaped single planar board. One of the most exhaustive parts of existing LiDAR calibration procedures is to manually find target objects from massive point clouds. To obviate user interventions, we propose an automated planar board detection from LiDAR range images. To extract a target completely, we suppress outliers and restore rejected inliers of the target board by introducing a target completion method. We empirically find that range measurements of various LiDARs are mainly skewed by constant offset values. To compensate for this, we suggest a range offset model for each laser channel in calibration procedures. The relative pose between LiDARs and range offsets are jointly estimated by minimizing bi-directional point-to-board distances within the iterative re-weighted least squares (IRLS) framework. To verify the suggested range offset model, we obtain and analyze extensive real-world measurements. By conducting experiments using the various sensor configurations and shapes of boards, we quantitatively and qualitatively confirm accuracy and versatility of the proposed method by comparing with the state-of-the-art LiDAR calibration methods. All the source code and data used in the paper are available at : <https://github.com/JunhaAgu/AutoL2LCalib>.

## I. INTRODUCTION

3D light detection and ranging sensor (LiDAR) has gained popularity in various fields including autonomous driving and robotics, thanks to its capability to provide real-time omnidirectional 3D point clouds. Despite the continued advance in the LiDAR technology, point clouds from a LiDAR are usually very sparse within a narrow field of view (FOV) limit. To obtain denser and wider representations, exponentially high cost becomes a prohibitive factor in most practical deployments.

To obtain a cost-efficient dense LiDAR representation, multi-LiDAR systems are widely employed in most autonomous systems [1]–[3]. Because the performance of algorithms using the multi-LiDAR system heavily depends on an accuracy of relative poses of LiDARs, such as tracking [2] object and detection [3] using multiple LiDARs, an accurate extrinsic calibration between multiple LiDARs is essential to seamlessly utilize all the measurements.

In this paper, we propose a self-contained LiDAR-based extrinsic calibration method using LiDAR data only, with no additional sensors. We note that there are only few studies on LiDAR-based extrinsic calibration, and there still remain

This research was supported by a research grant from Hyundai Construction Equipment. All authors are with Department of Mechanical and Aerospace Engineering, Seoul National University and Automation and Systems Research Institute (ASRI), Seoul, South Korea. {wnsgk02,rslackd93,cat7945,hjinkim}@snu.ac.kr

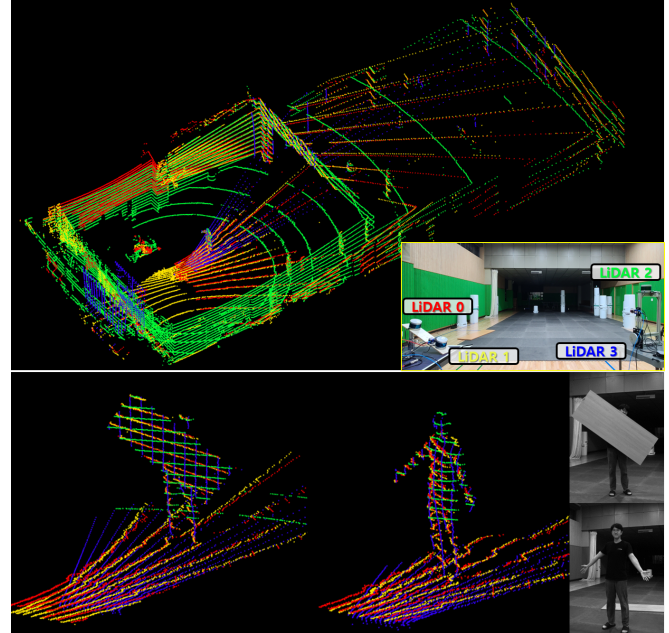


Fig. 1: The extrinsic calibration result of four LiDARs using the proposed calibration method. Each color indicates 3D point clouds from each LiDAR represented with the same color in the inset.

limitations. First, they apply only to a specific environment or the exact dimension of a target should be known [4], [14]–[17]. In addition, most existing methods require additional sensors for the extrinsic calibration in the multi-LiDAR setup [4], [6]–[8]. Due to the assumptions about the relative pose between multiple LiDARs, they can be employed only in simple configurations such as a horizontal mount [14], [17]. Thus, we aim to solve the aforementioned issues by proposing a new LiDAR-based calibration method.

## A. Related work

We categorize the extrinsic calibration methods for sensor systems including LiDARs into two approaches: 1) motion-based methods that estimate relative poses of sensors by aligning an estimated trajectory from independent sensors or fused sensor information, and 2) target-based methods that use specific targets.

Among the motion-based methods, [10], [11] introduces calibration methods for heterogeneous sensors by using trajectories and maps. Because the motion-based calibration approach requires estimated trajectories in each sensor, the results of this method depend on qualities of the estimated motions. In addition, these algorithm can not perfectly operate without cameras. In [12], they proposed motion-based calibration for systems including LiDARs by using a sensor

fusion odometry. However, because they aim to improve the camera-motion estimation by adding LiDAR information, this algorithm also heavily depends on a vision sensor. A research work [13] also aligned the estimated motions of LiDARs in initialization step. Due to motion drifts, an additional refinement step is needed using targets with known dimensions.

The target-based methods exploit identifiable objects or precision-processed targets, and estimate the relative pose between sensors by aligning the target positions observed on each sensor [4], [8], [14]–[18]. A research work [4] estimates extrinsic parameters of multiple LiDARs using Apriltags [5]. In [8], a relative pose of dual LiDARs is estimated using known displacements of landmarks on poles. [14] used concentric circles of conic objects, and aligned the centers of circles measured in each sensor by using the iterative closest point (ICP) algorithm to calculate sensor poses. A method proposed by [15] also assumed that the radius of the target is exactly known in advance. Because both methods [14], [15] require exact dimensions of the radius of targets, the result can be affected by the accuracy of radius measurement.

Other approach [16] uses boxes with arbitrary dimensions as targets; however, their algorithm is based on a strong assumption that the three planes are perpendicular to each face. [9] presents an extrinsic calibration algorithm for 2D LiDARs using two orthogonal planes. Inspired by [9], a research work [17] extends the method for 3D LiDARs using three near-orthogonal planes. However, the algorithm can operate under assumptions that LiDARs are mounted horizontally and that three independent planes intersect at an exact point, which is not a general situation in real-world environments.

In summary, most existing LiDAR calibration methods mainly have four limitations: they 1) use targets with known dimensions or assume specific operating conditions, 2) demand user's manual interventions to detect and extract targets, 3) depend on external modules such as odometry or simultaneously localization and mapping (SLAM), and 4) require additional sensors such as inertial measurement units (IMU) [7], global positioning systems (GPS) [8], and vision sensors [4], [6]. Also, an extrinsic calibration method considering intrinsic parameters of LiDAR using only LiDAR measurements has not been proposed. To make self-contained LiDAR calibration system, in this paper, we aim to develop the extrinsic calibration using only LiDAR measurements without aid of external sensors.

## B. Contributions

In this paper, we propose an automatic and accurate extrinsic calibration algorithm for 3D LiDARs. The main contributions are as follows:

- We design an automated planar board extraction method by using range images, which can be applied to other planar target-based methods as a front-end.
- By incorporating a range offset model into estimation procedures, the overall accuracy of the estimated relative pose is improved.

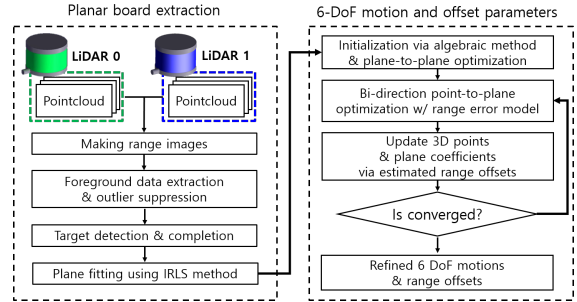


Fig. 2: The flowchart of the proposed algorithm.

- Our method only needs an arbitrary planar board.
- Through the extensive real-world experiments, we demonstrate that the proposed method shows more accurate calibration results compared to the state-of-the-art methods.

## C. Overview

A flow chart of the proposed method is represented in Fig. 2. In Section. III, to extract a planar board automatically, a ROI extraction method is represented by utilizing range images with respect to each azimuth and elevation angle. In addition, applying the techniques of the image process, we detect a target and through completion algorithm, we can restore the 3D target. In Section IV, we define the range error model with offsets and formulate the bi-directional joint optimization using the Huber weight. The extensive analysis of methods on core part and comparison with state-of-art calibration methods by using real-world experiment are following in Section. V.

## II. PRELIMINARIES

### A. Notations

Before presenting details of the proposed method, we briefly describe notations used in this paper. Bold letters represent column vectors and matrices. The reference LiDAR frame and the other LiDAR frame are denoted as  $\{L_0\}$  and  $\{L_1\}$ , respectively. The left superscript  $l$  indicates the LiDAR frame in which variables are represented. Without loss of generality in explanation, we describe dual LiDARs setting, i.e.  $l \in \{0, 1\}$ . For example, we denote the  $j$ -th 3D point of the  $i$ -th measurement sequence in the  $l$ -th LiDAR coordinate as  ${}^l \mathbf{X}_{i,j}$ . The coefficients of a plane equation are represented as  ${}^l \mathbf{N}_i = [{}^l a_i, {}^l b_i, {}^l c_i, {}^l d_i]^T \in \mathbb{R}^4$  where the first three elements of  ${}^l \mathbf{N}_i$  are defined as a unit normal vector  ${}^l \mathbf{n}_i = [{}^l a_i, {}^l b_i, {}^l c_i]^T \in \mathbb{R}^3$ . Then,  ${}^l d_i$  denotes the minimum distance between the origin and the plane. The plane can be represented as

$${}^l \mathbf{N}_i^\top {}^l \bar{\mathbf{X}}_{i,j} = {}^l \mathbf{n}_i^\top {}^l \mathbf{X}_{i,j} + {}^l d_i = 0, \quad (1)$$

where  ${}^l \bar{\mathbf{X}}_{i,j}$  is the homogeneous representation of  ${}^l \mathbf{X}_{i,j}$ .

### B. Transformation of a 3D plane

We define a 3D rigid body transformation from  $\{L_0\}$  to  $\{L_1\}$  as  $\mathbf{T}_{01} \in SE(3)$ . We can write down the dot product between a plane coefficient  ${}^0 \mathbf{N}_i$  and a 3D point  ${}^0 \bar{\mathbf{X}}$ ,

$${}^0 \mathbf{N}_i^\top {}^0 \bar{\mathbf{X}} = {}^0 \mathbf{N}_i^\top \mathbf{T}_{10}^{-1} \mathbf{T}_{10} {}^0 \bar{\mathbf{X}} = ({}^0 \mathbf{N}_i^\top \mathbf{T}_{10}^{-1}) (\mathbf{T}_{10} {}^0 \bar{\mathbf{X}}). \quad (2)$$

With  ${}^1\bar{\mathbf{X}} := \mathbf{T}_{10} {}^0\bar{\mathbf{X}}$ , we can deduce that  ${}^0\mathbf{N}_i^\top \mathbf{T}_{10}^{-1}$  should be a warped plane coefficient  ${}^1\tilde{\mathbf{N}}_i \in \mathbb{R}^4$  represented in  $\{L_1\}$ ,

$${}^1\tilde{\mathbf{N}}_i^\top := {}^0\mathbf{N}_i^\top \mathbf{T}_{10}^{-1} \longrightarrow {}^1\tilde{\mathbf{N}}_i = (\mathbf{T}_{10}^{-1})^\top {}^0\mathbf{N}_i = (\mathbf{T}_{01})^\top {}^0\mathbf{N}_i, \quad (3)$$

$$(\mathbf{T}_{01})^\top {}^0\mathbf{N}_i = \begin{bmatrix} \mathbf{R}_{01}^\top {}^0\mathbf{n}_i \\ \mathbf{t}_{01}^\top {}^0\mathbf{n}_i + {}^0d_i \end{bmatrix} \in \mathbb{R}^4. \quad (4)$$

In Eq. (4), a rotation motion only affects the normal vector part, and the unit length of the normal vector never changes:

$$\|{}^0\mathbf{n}_i\|_2 = \|{}^0\mathbf{n}_i\|_2 = 1. \quad (5)$$

### C. Relative Motion Estimation via Points and Planes

In this paper, we use 3D points and planes from the measured point clouds to estimate relative motions of LiDARs. There are mainly three ways to estimate the relative motion according to the employed geometric information: point-to-point [14], [16], plane-to-plane [17], and points-to-plane [9].

The point-to-point (*p2p*) method is known as the iterative closest points (ICP) algorithm [21]. It minimizes the distance of 3D points observed in each LiDAR. We can define a cost minimization problem with  $M_p$  points:

$$\mathbf{T}(\xi) : se(3) \mapsto SE(3), \quad (6)$$

$$\xi_{01}^* = \arg \min_{\xi \in se(3)} \sum_{j=1}^{M_p} \|\mathbf{T}_{01}(\xi) {}^1\bar{\mathbf{X}}_j - {}^0\bar{\mathbf{X}}_j\|_2 \in se(3). \quad (7)$$

However, to use this method the correspondences of points should be correctly established [14], which is not always guaranteed with 3D LiDARs due to their sparse point clouds.

The Kabsch algorithm [29] can be adopted to estimate a least-squares relative rotation by aligning a set of plane-to-plane (*P2P*) unit normal vectors with known correspondences,  ${}^0\mathbf{n}_i$  and  ${}^1\mathbf{n}_i$ . The cross-covariance matrix  $\Sigma_{\mathbf{n}_i {}^1\mathbf{n}_i}$  between normal vectors can be calculated as

$$\Sigma_{\mathbf{n}_i {}^1\mathbf{n}_i} = \frac{1}{N} \sum_{i=1}^N {}^0\mathbf{n}_i {}^1\mathbf{n}_i^\top, \quad (8)$$

where  $N$  denotes the number of measurement sequences. By the singular value decomposition (SVD), the cross-covariance matrix can be decomposed as  $\Sigma_{\mathbf{n}_i {}^1\mathbf{n}_i} = \mathbf{U}\mathbf{S}\mathbf{V}^\top$ , and the rotation matrix  $\mathbf{R}$  can be calculated as  $\mathbf{R} = \mathbf{U}\mathbf{V}^\top$ . Because a *P2P* version of the Kabsch algorithm can only provide a rotation motion, the optimization-based *P2P* can be designed to estimate a full 6-DoF motion as

$$\xi_{01}^* = \arg \min_{\xi \in se(3)} \sum_{i=1}^N \left\| \mathbf{T}_{01}(\xi)^\top {}^0\mathbf{N}_i - {}^1\mathbf{N}_i \right\|_2. \quad (9)$$

The points-to-plane (*p2P*) method estimates 6-DoF relative motion by minimizing normal distances from 3D points to a reference plane in 3D. The cost minimization problem can be formulated by a plane in 3D in  $\{L_0\}$  and points in  $\{L_1\}$  as

$$\xi_{01}^* = \arg \min_{\xi \in se(3)} \sum_{i=1}^N \sum_{j=1}^{M_p(i)} \left\| {}^0\mathbf{N}_i^\top \mathbf{T}_{01}(\xi) {}^1\bar{\mathbf{X}}_{i,j} \right\|_2, \quad (10)$$

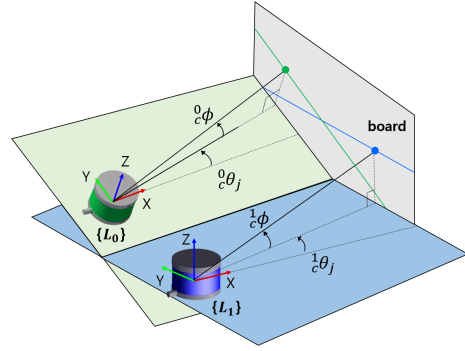


Fig. 3: **Coordinate frames of  $\{L_0\}$  and  $\{L_1\}$** . Elevation and azimuth angles are represented as  $(\phi)$  and  $(\theta)$ , respectively.

where  $M_p(i)$  denotes the total points in the  $i$ -th measurement sequence.

One advantage of *p2P* methods is that each point can be dealt with independently while in methods based on the plane-to-plane paradigm the points are only used to extract planes. We found that the *P2P*-based approach yields inaccurate estimations if outlier points are not properly suppressed when generating planes. Taking these into account, we explain our relative motion estimation approach in detail in Section IV-B.

## III. AUTOMATIC ROI DETECTION AND COMPLETION

In the existing methods [16], [17], [19], [20], interested target regions are known in advance, or need to be manually specified by users. To make this procedure autonomous, we propose an automatic ROI detection and completion method by using LiDAR range images.

### A. Generating range images from point clouds

First, 3D range data is represented in the 2D range image coordinate. We can calculate the elevation  $\phi$  and azimuth  $\theta$  angles by from range value  $\rho$  of a 3D point in the LiDAR coordinate frame as follows:

$$\theta_j = \arcsin(z_j/\rho_j) \quad (11)$$

$$\phi_j = \begin{cases} \arccos(\alpha_j) & \text{if } \alpha_j \geq 0, \beta_j \geq 0 \\ 2\pi - \arccos(\alpha_j) & \text{if } \alpha_j \geq 0, \beta_j < 0 \\ \pi - \arccos(\alpha_j) & \text{if } \alpha_j < 0, \beta_j \geq 0 \\ \pi + \arccos(\alpha_j) & \text{if } \alpha_j < 0, \beta_j < 0 \end{cases}, \quad (12)$$

where  $\alpha_j$  and  $\beta_j$  denote  $x_j / (\rho_j \cos \theta_j)$  and  $y_j / (\rho_j \cos \theta_j)$  respectively. By using vertical and horizontal resolutions of LiDARs, we can generate range images like Fig. 4. In the image, the horizontal step represents a real-world range value within an azimuth resolution and the vertical step corresponds to the elevation resolution.

### B. Initial ROI extraction via difference of range images

To detect ROI regions from range images, we first select a range image among data measurement as a reference image for comparing other range images as depicted in Fig. 4(a), and the rest of range images are regarded as query images as illustrated in Fig. 4(b). By subtracting the reference image from a query image, ROI candidate regions are extracted

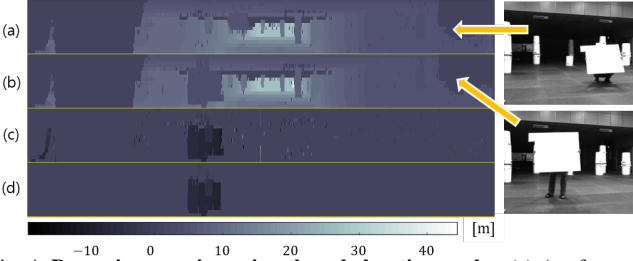


Fig. 4: Range image using azimuth and elevation angles. (a) A reference image of the dataset, (b) a query image, (c) a foreground image using difference between the reference and the query images, and (d) a final result after suppressing outliers.

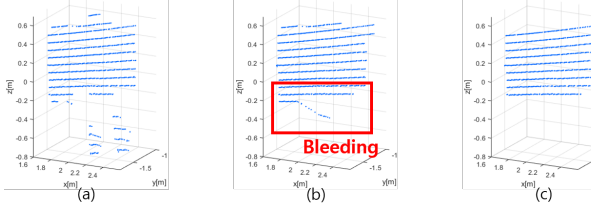


Fig. 5: The planar board extraction of 3D point clouds. (a) The result of the foreground extraction and outlier suppression in the range image of Fig. 4(d). (b) the result of the target detection and completion using the 3D plane RANSAC. (c) the result of the IRLS-based plane estimation.

from the foreground regions as shown in Fig. 4(c). To suppress pepper noise in the ROI candidate regions in Fig. 4(c), we erode the masked candidate regions, and fill the eroded regions by image morphological methods as Fig. 4(d). The masked regions are re-projected onto the 3D space for the planar board region completion step to be explained next.

### C. Completing detected ROI point clouds

Through the random sample consensus (RANSAC) algorithm for the 3D points re-projected with a plane model, the foreground points in Fig. 4(d) can be extracted and regarded as initial ROI candidate 3D points. We found that there are many holes in the resulting ROI of the RANSAC-based point extraction by wrongly rejected inlier points. To complete ROI detection results, 3D points are restored by using range continuities along each channel residing on a plate region.

To specify points belonging to planar regions, [22] utilizes the 3D continuity condition of consecutive points on a plane along a laser azimuth step direction. Inspired by this idea, we check range continuities of the previously extracted 3D points. To examine the continuity of 3D points on a plane, we set a threshold value  $\Delta\rho_{th}$  on ranges slightly larger than the range noise level reported in each sensor specification. Then, we repeatedly check whether two neighboring points of a query point are inside a sphere with radius  $\Delta\rho_{th}$  centered on the current query point. If the neighboring points are in the sphere, we include them into the inlier set, and restart the continuity checks for both points. This procedure ceases if one of the neighboring points of the current query point is outside of the sphere.

### D. Robust plane fitting via IRLS estimation

Due to the measurement ambiguities of sensor measurement on sharp edges of objects, bleeding points occur on boundaries of objects, and are regarded as false positives

in the continuity check step as illustrated in Fig. 5(b). To suppress the bleeding outliers and estimate the optimal plane coefficients  ${}^l\mathbf{N}_i^*$  of the  $i$ -th measurement sequence of the  $l$ -th LiDAR, we additionally solve an optimization-based plane fitting problem using the iterative re-weighted least squares (IRLS) as follows:

$${}^l\mathbf{N}_i^* = \arg \min_{{}^l\mathbf{N}_i \in \mathbb{R}^4} \sum_{j=1}^{M_p} w_H({}^l r_{i,j}) \in \mathbb{R}, \quad (13)$$

$${}^l r_{i,j} = \frac{{}^l a_i {}^l x_{i,j} + {}^l b_i {}^l y_{i,j} + {}^l c_i {}^l z_{i,j} + {}^l d_i}{\sqrt{{}^l a_i^2 + {}^l b_i^2 + {}^l c_i^2}}, \quad (14)$$

where the Huber norm  $w_H(\cdot)$  is used for robustness to the bleeding outliers. The optimized planes are used in the extrinsic relative motion estimation step in the following sections.

## IV. 6-DOF MOTION AND RANGE OFFSETS ESTIMATION

In this section, we analyze LiDAR measurements via real-world data acquisition, and introduce a range offset model for each laser channel of the LiDAR for more accurate estimation of calibration parameters. Then, we jointly estimate the 6-DoF relative pose between two LiDARs and the range offsets of each channel of each LiDAR by solving a bi-directional points-to-plane normal distance minimization problem.

### A. Range error modeling

One way to achieve more accurate extrinsic calibration is to consider intrinsic uncertainties of the LiDAR hardware. As reported in [24], the time uncertainty of electronic circuits induces skewed range measurements of laser-based sensors. To deal with this, several works [23]–[26] addressed that factory-calibrated parameters of a LiDAR can be further tuned by mathematically modeling range error factors and using additional sensors, such as calibrated cameras and targets with known dimensions, which significantly improves overall extrinsic calibration performance.

Two mathematical models for range measurement errors have been suggested in the previous works: 1) a constant range offset model [23] and 2) an affine range correction model [24]. The affine model can be denoted as below,

$$\rho_m = \alpha \rho_t + \Delta \rho. \quad (15)$$

where  $\rho_t, \rho_m \in \mathbb{R}$  are true and measured range values, and  $\alpha$  and  $\Delta \rho$  are scale and offset factors, respectively. If  $\alpha = 1$ , Eq. (15) becomes the constant range offset model.

To verify both models, we conduct real-world experiments to acquire distances between a Velodyne VLP-16 fixed on the ground and a large planar object with various displacements. The location of the object is carefully changed from 1.5 m to 10 m by 0.5 m step as depicted in Fig. 6(a). We calculate errors between the ground truth distances of the object and measured values, and illustrate error tendencies of selected four laser channels which are seen in all distances in Fig. 6(b). As can be seen in Fig. 6(b), constant offset errors dominantly affect the measurement distortions rather than the

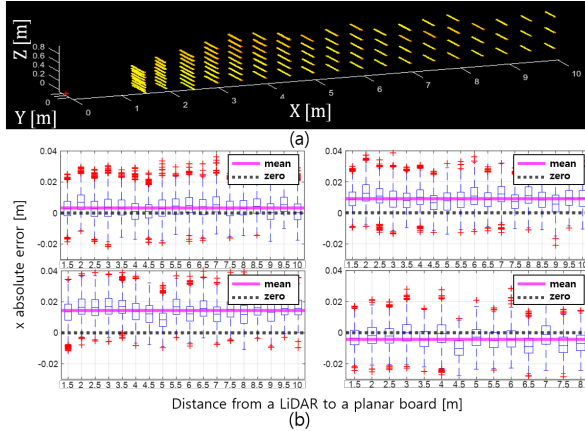


Fig. 6: **Absolute x error according to planar board distances.** We obtain hundreds of range measurements for 1 m × 1 m planar board along the x-axis of a LiDAR by 0.5 m intervals. We calculate means and standard deviations of x error at each distance of planar board. The x error values of the 9-th, 10-th, 11-th and 12-th channels are plotted in the order of the top left, top right, bottom left, and bottom right.

scale factor, and each laser channel is governed by different constant values.

Thus, we adopt the range offset model in Eq. (16) to represent intrinsic distortions of range measurements of each laser channel. We can derive a range offset model for the extrinsic calibration of LiDARs as  ${}^l_c\rho^* = {}^l_c\rho_j + {}^l_c\Delta\rho$  and each point can be represented as follows:

$${}^l_c\mathbf{x}_{i,j}^* = \begin{bmatrix} {}^l_cx_{i,j}^* \\ {}^l_cy_{i,j}^* \\ {}^l_cz_{i,j}^* \end{bmatrix} = {}^l_c\mathbf{x}_{i,j} + {}^l_c\Delta\rho \begin{bmatrix} \cos({}^l_c\phi) \cos({}^l_c\theta_j) \\ \cos({}^l_c\phi) \sin({}^l_c\theta_j) \\ \sin({}^l_c\phi) \end{bmatrix}, \quad (16)$$

where  $c$  denotes a  $c$ -th channel of  $l$ -th LiDAR. With this model, we design an optimization problem to jointly estimate range offsets and extrinsic relative poses of sensors by only using LiDAR measurements.

### B. Parameter estimation via bi-directional cost minimization

In this section, we estimate the relative pose and offset parameters of LiDARs via a bi-directional points-to-plane distances minimization problem. To start near a global minimum, we use the Kabsch algorithm [29] with the normal vectors in Section II-C to algebraically obtain the rotation motion, and the initial 6-DoF pose is estimated by the plane-to-plane method in Eq. (9).

We define a range offset vector for the  $l$ -th LiDAR as  ${}^l\mathbf{q} = [{}^l\Delta\rho, \dots, {}^{c_l}\Delta\rho]^T \in \mathbb{R}^{c_l}$  where  $c_l$  is the number of laser channels of the  $l$ -th LiDAR. Without loss of generality, we describe a problem for two LiDARs,  $\{L_0\}$  and  $\{L_1\}$ , then a parameter vector including the relative pose  $\xi_{01} \in se(3)$  and all offset values can be denoted as  $\mathbf{s} = [\xi_{01}^T, {}^0\mathbf{q}^T, {}^1\mathbf{q}^T]^T \in \mathbb{R}^{6+c_0+c_1}$ . We define a residual value  ${}^0r_{i,j} \in \mathbb{R}$  as

$${}^0r_{i,j} := {}^1\mathbf{N}_i^\top \mathbf{T}(\xi_{01})^{-1} {}^0\mathbf{X}_{i,j}^*, \quad (17)$$

where  ${}^0\mathbf{X}_{i,j}^*$  represents the  $j$ -th 3D query point of the  $i$ -th measurement sequence of LiDAR0, and  ${}^1\mathbf{N}_i$  represents the corresponding  $i$ -th 3D reference plane in  $\{L_1\}$ . Eq. (17) can be interpreted as a normal distance of  ${}^0\mathbf{X}_{i,j}^*$  and  ${}^1\mathbf{N}_i$ .

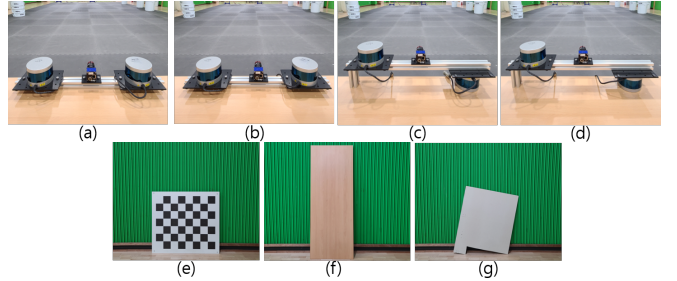


Fig. 7: **Four configurations of two LiDARs and three boards for evaluations.** (a) 0.4 m displacement y-direction from the left LiDAR, (b) same displacement with a right LiDAR rotated by 45 deg, (c) 180-deg-flipped right LiDAR with 0.4 m displacement, (d) additional 45-deg rotation of a right LiDAR. (e) A checkerboard, (f) a long board, and (g) a cut board.

Analogously, by swapping the roles of reference and query LiDARs each other, we can define a residual value  ${}^1r_{i,j}$  as

$${}^1r_{i,j} := {}^0\mathbf{N}_i^\top \mathbf{T}(\xi_{01}) {}^1\mathbf{X}_{i,j}^*. \quad (18)$$

With both bi-directional normal distances, we can define a residual vector  $\mathbf{r} \in \mathbb{R}^{{}^0N_t + {}^1N_t}$  as

$$\mathbf{r} = [{}^0r_{1,1}, \dots, {}^0r_{N, {}^0M_p(N)}, {}^1r_{1,1}, \dots, {}^1r_{N, {}^1M_p(N)}]^\top, \quad (19)$$

where  $N$  denotes the total sequences and  ${}^lM_p(i)$  is the number of points belonging to the  $i$ -th sequence of the  $l$ -th LiDAR, and  ${}^lN_t = \sum_{i=1}^N {}^lM_p(i)$  denotes the total number of points of the  $l$ -th LiDAR. A cost minimization problem estimating the optimal solution  $\mathbf{s}^*$  can be formulated as

$$\mathbf{s}^* = \arg \min_{\mathbf{s}} \mathbf{r}^\top \mathbf{W} \mathbf{r}, \quad (20)$$

where  $\mathbf{W} \in \mathbb{R}^{{}^0N_t + {}^1N_t} \times {}^0N_t + {}^1N_t$  is a Huber weighting matrix. Then, with the Jacobian matrix

$$\mathbf{J} = \begin{bmatrix} \frac{\partial \mathbf{r}}{\partial \xi_{01}} & \frac{\partial \mathbf{r}}{\partial {}^0\mathbf{q}} & \frac{\partial \mathbf{r}}{\partial {}^1\mathbf{q}} \end{bmatrix} \in \mathbb{R}^{{}^0N_t + {}^1N_t} \times (6 + c_0 + c_1), \quad (21)$$

the update  $\delta\mathbf{s} \in \mathbb{R}^{6+c_0+c_1}$  can be calculated by the Gauss-Newton method as

$$\delta\mathbf{s} = -(\mathbf{J}^\top \mathbf{W} \mathbf{J})^{-1} \mathbf{J}^\top \mathbf{W} \mathbf{r}. \quad (22)$$

The optimization parameters are iteratively updated,

$$\mathbf{s} \leftarrow \mathbf{s} + \delta\mathbf{s}, {}^l\mathbf{x}_{i,j} \leftarrow {}^l\mathbf{x}_{i,j}^*. \quad (23)$$

Note that since the updated offsets change the measured 3D point coordinates, the plane coefficients should be updated by Eq. (16) at every iteration. This process continues until the convergence.

## V. EXPERIMENT RESULTS

This section provides details on our experiment with real-world data and evaluate the overall performance of the proposed method.

### A. Settings

For our experiments, we use four 16-channel Velodyne Puck LiDARs with 10 Hz measurement rate. To show the compatibility of the proposed method for arbitrary sensor configurations, we set five placement settings as depicted in Figs. 7(a)–(d) and 10. Besides, three different planar boards are used to show that the proposed method can operate with any arbitrary planar board as shown in Figs. 7(e)–(g).

TABLE I: **Qualitative evaluations** - rotation  $\mathbf{R}_{01}$  and translation  $\mathbf{t}_{01}$  errors of the estimated relative pose in configuration 1-4. The rotation represents yaw, pitch, and roll in order and the translation represents x, y, z in order. The errors are calculated by the relative pose error (RPE) [30]. A checkerboard is used for configurations 1 and 2, and three different types of planar boards are used for configurations 3 and 4. \* means diverging.

Method	Configuration 1				Configuration 2			
	$\mathbf{R}_{01}$ error [deg]	norm [deg]	$\mathbf{t}_{01}$ error [cm]	norm [cm]	$\mathbf{R}_{01}$ error [deg]	norm [deg]	$\mathbf{t}_{01}$ error [cm]	norm [cm]
dual [17]	-0.06, -0.04, -0.01	0.07	0.56, 1.36, -0.92	1.74	0.15, 0.21, 0.18	0.32	0.87, 0.33, -1.05	1.40
motion [11]	0.31, 0.04, -0.07	0.32	5.41, 1.96, 0.31	5.76	-0.42, -0.18, 0.06	0.46	-4.11, 5.04, -1.94	6.79
L2C [28]	-0.01, 0.04, -0.01	<b>0.04</b>	0.38, 0.32, -0.46	0.67	1.55, 0.47, -0.01	1.62	0.03 -0.80 -0.63	1.02
proposed w/o $\Delta\rho$	-0.09, -0.33, 0.59	0.68	0.59, -0.36, -2.54	2.63	0.12 0.01 0.38	0.40	0.40 0.1 -1.75	1.80
proposed	0.04, 0.06, 0.48	0.49	0.01, -0.32, -0.07	<b>0.36</b>	0.12, 0.21, 0.11	<b>0.27</b>	0.16, -0.33, -0.04	<b>0.37</b>
Configuration 3								
Method	$\mathbf{R}_{01}$ error [deg]	norm [deg]	$\mathbf{t}_{01}$ error [cm]	norm [cm]	$\mathbf{R}_{01}$ error [deg]	norm [deg]	$\mathbf{t}_{01}$ error [cm]	norm [cm]
dual [17]	179, -15.4, -179	254*	31.3, 14.1, 216	219*	-64.6, 16.6, 170.0	182*	33.1, 4.06, 158	162*
motion [11]	-0.04, -0.08, 1.15	1.15	2.09, 3.13, 0.02	3.77	-0.63, -0.50, -0.6	1.00	6.45, 0.10, -6.27	9.00
L2C [28]	0.43, 0.02, 0.35	0.56	0.35, -0.73 0.59	1.00	0.04, -0.01, 0.12	<b>0.13</b>	0.18 -0.28 -0.53	<b>0.63</b>
proposed - checker	0.43, -0.19, 0.31	0.57	1.33, -0.84, 0.43	1.63	0.22, -0.18, 0.08	0.30	1.01, -1.37, -0.01	1.70
proposed - cut	0.68, 0.31 , 0.01	0.74	-0.56, -1.15, 1.62	2.06	0.72, -0.01, 0.32	0.79	-0.63, -1.23, 0.97	1.69
proposed - long	0.41, -0.10, 0.13	<b>0.44</b>	0.2, -0.63, -0.15	<b>0.68</b>	0.39, -0.27, 0.01	0.48	0.30, -1.71, -0.86	1.94

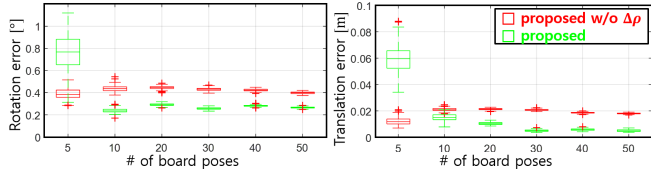


Fig. 8: **Rotation and translation error.** The red and green box plots indicate the proposed method without considering the range offset model and with the model, respectively. The rotation and translation errors of the relative pose are calculated by the relative pose error (RPE) proposed in [30]. The configuration 2 and the checkerboard are used.

### B. Effect of the range offset model

In this analysis, we evaluate the effect of the range offset model on the accuracy of the extrinsic calibration by changing the number of the board poses. Fig. 8 shows that the error of both methods decreases as the number of poses of the target board increases. However, it can be seen that the error of the proposed method with the model decreases more rapidly and becomes more accurate as the number of sequences increases. With the model, the proposed method optimizes more optimization variables than the method without the model. When the number of measurement sequences is not sufficient (for example, when the number of board poses is 5), an overfitting problem may appear. However, with enough measurements, the incorporation of the range offset model yields the significant performance enhancement as shown in Fig. 8. The estimated offset values of two LiDARs from the configurations 1–4 are plotted in Fig. 9.

### C. Performance comparison

We conduct experiments for five configurations as shown in Figs. 7(a)–(d) and Fig. 10, and compare the proposed method with the three other state-of-art of LiDAR calibration methods in both qualitative and quantitative perspectives.

For comparison, first, a dual LiDAR calibration method [17] is used, which is the latest study that has published the code among the studies on the extrinsic calibration of LiDARs. Then, for comparison with the motion-based method, we obtain the trajectory and map using LeGo-LOAM [27] and utilize the motion-based calibration method [11]. Lastly, we compare with the camera-to-LiDAR calibration for the relative pose of LiDARs. Although this is not a method that uses data of LiDARs only, the relative pose between LiDARs can be obtained through the camera-to-LiDARs calibration. We implemented one of the state-of-art LiDAR-to-camera calibration methods [28] for this.

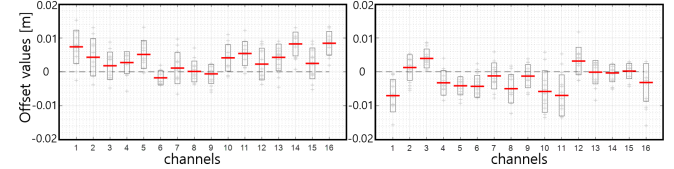


Fig. 9: **The estimated offset value** The left and right plots shows the offsets of LiDAR0 and LiDAR1, respectively estimated from configurations 1–4.

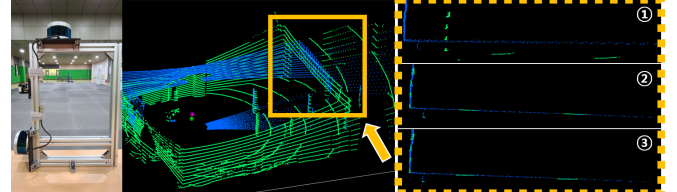


Fig. 10: **Qualitative results of a complex configuration.** Each number indicates motion-based [11], L2C [28] and the propose method in order. Note that dual [17] does not operate in this configuration.

The comparison results are shown in Table I and Fig. 10. Due to motion drifts, the overall performance of the motion-based method [11] is not good. According to the results of configurations 1–2 and a complex setting shown in Fig. 10, it is noted that compared with the L2C [28] method, the proposed method shows competitive performance without additional sensors. The results of configurations 3–4 show that the proposed method can operate with any arbitrary planar board and has comparable performance with the others. Note that in configurations 3–4, the dual method [17] fails to operate because it requires the assumption that two LiDARs are horizontally mounted. These results confirm that the proposed method has competitive performance compared to other the-state-of-art methods, with enhanced practicability.

## VI. CONCLUSIONS

In this paper, we presented an automated extrinsic calibration method for a multi-LiDAR setup with the range offset model. We proposed the automated planar board extraction method which has the applicability with planar target-based calibration methods as a front-end. The proposed method can operate using only an arbitrary planar board without the need for a precisely processed target such as a checkerboard, and can be implemented in any LiDAR configuration. With integration of the range offset model into the extrinsic calibration process, we demonstrated the accurate performance of our method by comparing with the other state-of-the-art methods, both quantitatively and qualitatively.

## REFERENCES

- [1] A. Rangesh and M. M. Trivedi, "No blind spots: full-surround multi-object tracking for autonomous vehicles using cameras and lidars," *IEEE Transactions on Intelligent Vehicles*, vol. 4, no. 4, Dec. 2019, pp. 588-599.
- [2] M. Sualeh and G. W. Kim, "Dynamic multi-lidar based multiple object detection and tracking," *Sensors*, vol. 19, no. 6, March 2019, p. 1474.
- [3] J. Jiao, P. Yun, L. Tai, and M. Liu, "MLOD: awareness of extrinsic perturbation in multi-lidar 3d object detection for autonomous driving," IEEE/RSJ International Conference on Intelligent Robots and Systems (IROS), 2020.
- [4] Y. Xie, R. Shao, P. Guli, B. Li, and L. Wang, "Infrastructure based calibration of a multi-camera and multi-lidar system using apriltags," IEEE Intelligent Vehicles Symposium (IV), 2018.
- [5] E. Olson, "Apriltag: A robust and flexible visual fiducial system," IEEE International Conference on Robotics and Automation (ICRA), 2011.
- [6] G. Xie, T. Xu, C. Isert, M. Aeberhard, S. Li, and M. Liu, "Online active calibration for a multi-lrf system," IEEE International Conference on Intelligent Transportation Systems (ITS), 2015.
- [7] M. He, H. Zhao, F. Davoine, J. Cui, and H. Zha, "Pairwise lidar calibration using multi-type 3d geometric features in natural scene," IEEE/RSJ International Conference on Intelligent Robots and Systems (IROS), 2013.
- [8] G. Chao and J. R. Spletzer, "On-line calibration of multiple lidars on a mobile vehicle platform," IEEE International Conference on Robotics and Automation (ICRA), 2010.
- [9] D. Choi, Y. Bok, J. Kim, and I. S. Kweon, "Extrinsic calibration of 2-D lidars using two orthogonal planes," *IEEE Transactions on Robotics*, vol. 32, no. 1, Feb. 2016, pp. 83-98.
- [10] Z. Taylor and J. Nieto, "Motion-based calibration of multimodal sensor arrays," IEEE International Conference on Robotics and Automation (ICRA), 2015.
- [11] Z. Taylor and J. Nieto, "Motion-based calibration of multimodal sensor extrinsics and timing offset estimation," *IEEE Transactions on Robotics*, vol. 32, no. 5, Oct. 2016, pp. 1215-1229.
- [12] R. Ishikawa, T. Oishi, K. Ikeuchi, "LiDAR and camera calibration using motions estimated by sensor fusion odometry," IEEE/RSJ International Conference on Intelligent Robots and Systems (IROS), 2018.
- [13] J. Jiao, Y. Yu, Q. Liao, H. Ye, R. Fan, and M. Liu, "Automatic calibration of multiple 3d lidars in urban environments," IEEE/RSJ International Conference on Intelligent Robots and Systems (IROS), 2019.
- [14] T. Kim and T. Park, "Calibration method between dual 3D lidar sensors for autonomous vehicles," IEEE Conference of the Society of Instrument and Control Engineers of Japan, 2017.
- [15] B. Xue, J. Jiao, Y. Zhu, L. Zhen, D. Han, M. Liu, and R. Fan, "Automatic calibration of dual-lidars using two poles stickered with retro-reflective tape," IEEE International Conference on Imaging Systems and Techniques, 2019.
- [16] Z. Pusztai and L. Hajder, "Accurate calibration of lidar-camera systems using ordinary boxes," IEEE International Conference on Computer Vision Workshops (ICCVW), 2017.
- [17] J. Jiao, Q. Liao, Y. Zhu, T. Liu, Y. Yu, R. Fan, L. Wang, and M. Liu, "A novel dual-lidar calibration algorithm using planar surfaces," IEEE Intelligent Vehicles Symposium (IV), 2019.
- [18] J. Kim, C. Kim, H. J. Kim, "Robust extrinsic calibration for arbitrarily configured dual 3D Lidars using a single planar board," IEEE International Conference on Control, Automation and Systems (ICCAS), 2020.
- [19] L. Zhou, Z. Li, and M. Kaess, "Automatic extrinsic calibration of a camera and a 3d lidar using line and plane correspondences," IEEE/RSJ International Conference on Intelligent Robots and Systems (IROS), 2018.
- [20] S. Verma, J. S. Berrio, S. Worrall, and E. Nebot, "Automatic extrinsic calibration between a camera and a 3d Lidar using 3d point and plane correspondences," IEEE Intelligent Transportation Systems Conference (ITSC), 2019.
- [21] Y. Chen and G. Medioni, "Object modelling by registration of multiple range images," *Image and Vision Computing*, vol. 10, no. 3, April 1992, pp. 145-155.
- [22] A. Kassir and T. Peynot, "Reliable automatic camera-laser calibration," Australasian Conference on Robotics and Automation, 2010.
- [23] G. Pandey, J. McBride, S. Savarese, and R. Eustice, "Extrinsic calibration of a 3d laser scanner and an omnidirectional camera," *IFAC Proceedings Volumes*, vol. 43, issue. 16, 2010, pp. 336-341.
- [24] F. M. Mirzaei, D. G. Kottas, and S. I. Roumeliotis, "3d lidar-camera intrinsic and extrinsic calibration: identifiability and analytical least-squares-based initialization," *The International Journal of Robotics Research*, vol. 31, no. 4, April 2012, pp. 452-467.
- [25] C. Y. Chen and H.-J. Chien, "On-site sensor recalibration of a spinning multi-beam lidar system using automatically-detected planar targets," *Sensors*, vol. 12, no. 10, Oct. 2012, pp. 13736-13752.
- [26] C. L. Glenniea, A. Kusaria, and A. Facchib, "Calibration and stability analysis of the vlp-16 laser scanner," *ISPRS Annals of Photogrammetry, Remote Sensing and Spatial Information Sciences*, 2016.
- [27] T. Shan and B. Englot, "Lego-loam: lightweight and ground-optimized lidar odometry and mapping on variable terrain," IEEE/RSJ International Conference on Intelligent Robots and Systems (IROS), 2018.
- [28] E. Kim and S. Park, "Extrinsic calibration between camera and lidar sensors by matching multiple 3d planes," *Sensors*, vol. 20, no. 1, 2020.
- [29] W. Kabsch, "A solution for the best rotation to relate two sets of vectors," *Acta Crystallographica Section A: Crystal Physics, Diffraction, Theoretical and General Crystallography*, vol. 32, no. 5, Sep. 1976, pp. 922-923.
- [30] J. Sturm, N. Engelhard, F. Endres, W. Burgard, and D. Cremers, "A benchmark for the evaluation of rgb-d slam systems," IEEE/RSJ International Conference on Intelligent Robots and Systems (IROS), 2012.